Materials Advances

ROYAL SOCIETY OF CHEMISTRY

PAPER

View Article Online
View Journal | View Issue

Cite this: *Mater. Adv.*, 2020, **1**, 1092

Boosted carrier mobility and enhanced thermoelectric properties of polycrystalline $Na_{0.03}Sn_{0.97}Se$ by liquid-phase hot deformation†

Hao Sun,[ab] Chang Tan,[b] Xiaojian Tan,[*b] Hongxiang Wang,[b] Yinong Yin,[b] Yuexin Song,[ab] Guo-Qiang Liu,[b] Jacques G. Noudem,[c] Quanguo Jiang,[a] Jianfeng Zhang,[a] Huajie Huang[*a] and Jun Jiang[*b]

Received 10th June 2020,
Accepted 29th June 2020

DOI: 10.1039/d0ma00405g

rsc.li/materials-advances

SnSe emerges as a promising thermoelectric material due to an ultrahigh *ZT* value in its single crystal while polycrystalline SnSe offers much lower *ZT*s resulting from the weak texturing degree. Here, we report a liquid-phase hot deformation technique to enhance the texturing degree of polycrystalline $Na_{0.03}Sn_{0.97}Se$, leading to a significantly boosted carrier mobility of 30.1 $cm^2\ V^{-1}\ s^{-1}$ at room temperature and a remarkable average power factor of 5.73 $\mu W\ cm^{-1}\ K^{-2}$ between 300 and 830 K. Moreover, the liquid-phase hot deformation procedure introduces dense dislocation defects and realizes an obviously reduced lattice thermal conductivity of 0.40 $W\ m^{-1}\ K^{-1}$ at 747 K. Consequently, a peak *ZT* of 0.9 at 780 K and a high average ZT_{ave} of 0.49 from 300 to 830 K were obtained for the polycrystalline $Na_{0.03}Sn_{0.97}Se$ sample. This work indicates that liquid-phase hot deformation is a convenient and energy-saving strategy to enhance the texturing degree and improve the thermoelectric performance in polycrystalline SnSe materials.

1. Introduction

In the last few decades, thermoelectric (TE) materials have drawn great attention due to their capacity of direct conversion between heat and electricity.[1–5] The conversion efficiency of TE materials is quantified by the dimensionless figure of merit $ZT = \alpha^2\sigma T/\kappa$, where α is the Seebeck coefficient, σ is the electrical conductivity, κ is the thermal conductivity (including the carrier κ_e and lattice κ_l contributions), and T is the operating temperature. The excellent TE performance could be realized by increasing the power factor (PF = $\alpha^2\sigma$) or compressing the thermal conductivity as much as possible.[6–8] Usually, several strategies such as resonant doping,[9,10] band convergence[11–13] and carrier concentration optimization[14,15] can effectively increase the power factor, while the lattice thermal conductivity κ_l can be reduced by the all-scale hierarchical structuring[16–19] and dense defects[20–23] as phonon scattering centers.

As an emerging TE material, the earth-abundant and environmentally-friendly binary compound tin selenide (SnSe) has attracted widespread attention owing to its intrinsic ultra-low thermal conductivity[24–26] and record-high *ZT* values for both p-type (2.6 at 923 K)[27] and n-type (2.8 at 773 K)[28] SnSe single crystals. Although the SnSe single crystals exhibit high *ZT*s, their poor mechanical properties severely limit their practical application in devices. Given this, polycrystalline SnSe has been expected to improve the mechanical properties, but their corresponding *ZT*s are much lower than those of the single crystals.[29–37] This is mainly because of their low oriented degree in polycrystalline samples, in other words, the poor texturing degree of polycrystalline SnSe leads to low electrical conductivity. Many previous studies have shown that the preferred orientation of polycrystalline SnSe grains is beneficial for improving the electronic transport properties.[38,39] The widely-used zone melting (ZM) is an efficient method to obtain good orientation, but the products still had poor mechanical properties.[40,41] Therefore, there is a need to develop advanced textured sintering methods to prepare polycrystalline SnSe samples with good orientation and mechanical properties.

The liquid-phase sintering (LPS) method was successfully used to enhance the texturing degree and mechanical properties of layered TE materials, such as $Bi_{0.5}Sb_{1.5}Te_3$ and SnSe.[42,43] For example, the Na-doped SnSe polycrystalline samples were surrounded by the liquid phase of Te during the sintering

[a] *College of Mechanics and Materials, Hohai University, Nanjing, 211100, China. E-mail: huanghuajie@hhu.edu.cn*
[b] *Ningbo Institute of Materials Technology and Engineering, Chinese Academy of Sciences, Ningbo 315201, China. E-mail: tanxiaojian@nimte.ac.cn, jjun@nimte.ac.cn*
[c] *Normandie University, ENSICAEN, UNICAEN, CNRS, CRISMAT, Caen 14000, France*

† Electronic supplementary information (ESI) available. See DOI: 10.1039/d0ma00405g

process. The optimized orientation led to a greatly improved PF_{ave} of 6.01 μW cm^{-1} K^{-2} and a higher ZT_{ave} of 0.45 between 300 and 830 K.[43] Besides, the hot deformation (HD) process was also applied to promote grain alignment and enhance texture modulation in Na-doped SnSe polycrystalline samples. Resulting from the increased μ_H by texturing in the HD process, a peak ZT value of 1.3 was achieved with a high PF of 10.2 μW cm^{-1} K^{-2}.[44] Obviously, both LPS and HD processes contribute to texture modulation and result in better electronic properties as well as mechanical properties in SnSe-based materials. Nevertheless, the HD procedure is somewhat complicated and energy-consuming with poor repeatability,[44–48] while the LPS process may induce a higher thermal conductivity.[43,49–51]

Recently, the liquid-phase hot deformation (LPHD) technique was proposed in n-type $Bi_2(Te,Se)_3$ alloys.[52] This unconventional process combined the advantages of LPS and HD closely, generating the excellent TE properties. In this work, we used the LPHD method to prepare polycrystalline SnSe-based materials. During the sintering process, the $Na_{0.03}Sn_{0.97}Se$ solid grains were initially surrounded by the liquid phase Te. Meanwhile, the prepared samples were gradually deformed in a larger graphite die with the extrusion of liquid phase Te. The recrystallization and orientation optimization of grains occurred by plastic deformation. As a result, an enhanced carrier mobility μ_H and a reasonably reduced lattice thermal conductivity were realized for the enhancement of TE properties in the LPHD polycrystalline $Na_{0.03}Sn_{0.97}Se$ samples.

2. Experimental details

2.1 LPHD synthesis of polycrystalline $Na_{0.03}Sn_{0.97}Se$

Polycrystalline $Na_{0.03}Sn_{0.97}Se$ samples alloyed with different Te ratios (x = 0, 5 and 15 wt%) were prepared by melting high-purity raw materials in stoichiometric ratios (Sn granules, 5 N; Se granules, 5 N; Na chunk, 3 N; Te chunk, 5 N) in 10 mm vacuum-sealed quartz tubes (10^{-4} Torr). The mixtures were melted at 1193 K for 1 h in the rocking furnace, ensuring composition homogeneity. The quartz tubes were then kept upright and air-cooled to form regular bulks. The obtained conical ingots were planished up and down to the cylinders (about 30 mm in height and 10 mm in diameter), and directly hot-deformed in larger ϕ 16 mm graphite dies at 753 K under 60 MPa for 15 min parallel to the circular axis direction of the cylinder. In particular, in order to ensure Te extrusion and HD occurring simultaneously, the ingots stayed at 725 K (melting point of Te) for 5 min, and then pressure was applied slowly. Finally, the high-density LPHD samples of 8 mm in height and 16 mm in diameter were obtained.

2.2 Characterization

The phase structures and grain orientation were characterized by X-ray diffraction (XRD, Bruker D8, Germany), using Cu K_α radiation (λ = 1.5406 Å). The chemical compositions and morphology were determined using energy dispersive spectroscopy (EDS, HKL MAX, Oxford Instruments) and scanning electron microscopy (SEM, Quanta FEG 250, FEI Co), respectively. The microstructures were investigated by using transmission electron microscopy (TEM, JEOL2100 HR).

2.3 Thermoelectric measurements

The electrical conductivity (σ) and Seebeck coefficient (α) were measured simultaneously using a ZEM-3 (Ulvac-Riko, Japan) from 300 to 830 K in a helium atmosphere. The thermal conductivity was determined by $\kappa = \rho C_P D$, where ρ is the sample density, C_P is the specific heat capacity, and D is the thermal diffusivity. The density ρ was measured using the Archimedes principle, the thermal diffusivity D was measured using the laser flash method (Netzsch, LFA-457, Germany), and the specific heat capacity C_p was obtained from previous reports.[27] Both the electronic and thermal transport properties were measured perpendicular to the pressure direction. The carrier concentration (n) and mobility (μ) were obtained from $n = 1/eR_H$ and $\mu = \sigma R_H$, where the Hall coefficient R_H was measured using a physical properties measurement system (Quantum Design, PPMS-9, US).

3. Results and discussion

3.1 XRD and morphology characterization

Fig. 1a shows the powder XRD patterns of the $Na_{0.03}Sn_{0.97}Se$–x%Te (x = 0, 5 and 15) polycrystalline samples at different prepared processes, including the loose melted bulk before HP, the dense sintered bulks after LPHD, and the ejected materials during the LPHD process. Before HP, the main peaks of SnSe (JCPDS #48-1224) and elemental Te (JCPDS #36-1452) appeared. After HP, there were only peaks for the SnSe phase observed because of the reason that the elemental Te was "squeezed out" during the LPHD process. As shown in Fig. S1 of the ESI,† the extrudate in the x = 15 sample was more than that in the x = 5 sample. Consistent with previous reports,[42,43,49] the extrudate was also elemental Te as observed from the XRD results.

The XRD patterns for the bulk samples were measured on the surface perpendicular to the pressure direction as shown in Fig. 1b. All diffraction peaks can be indexed to the orthorhombic phase with a space group *Pnma* phase without any obviously detectable second phase. It can be seen that the intensities of the (400) and (111) reflection peaks were different among these samples, suggesting that the preferred orientation of LPHD samples seems to be parallel to the (400) plane. Moreover, the

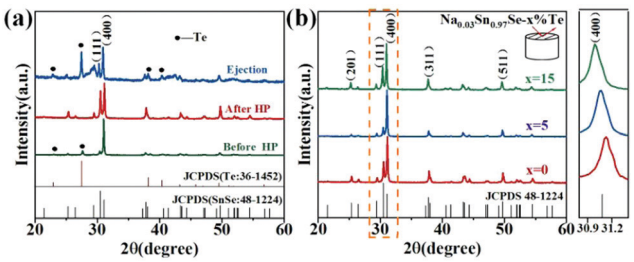

Fig. 1 (a) Powder XRD patterns for $Na_{0.03}Sn_{0.97}Se$–5%Te in different processes; (b) bulk XRD patterns for $Na_{0.03}Sn_{0.97}Se$–x%Te (x = 0, 5 and 15) measured on the surface perpendicular to the pressing direction.

Table 1 The density ρ, relative density and orientation factor $F(400)$ for the $Na_{0.03}Sn_{0.97}Se$–x%Te LPHD bulk samples

Samples (x content)	ρ (g cm^{-3})	Relative density (%)	$F(400)$
x = 0	5.76	93.1	0.26
x = 5	6.03	97.5	0.50
x = 15	6.08	98.5	0.32

(400) peaks shifted toward lower angles with the increasing Te content, which probably results from the thimbleful of Te atoms which entered the Se sites and thereby increased the unit cell volume (see Fig. S2 of the ESI†).

To evaluate the texture degree of the $Na_{0.03}Sn_{0.97}Se$–x%Te LPHD samples, the orientation factor F of the (hkl) plane was calculated using the Lotgering method by the following equations:

$$F = \frac{(P - P_0)}{(1 - P_0)} \quad (1)$$

$$P_0 = \frac{\sum I_0(00l)}{\sum I_0(hkl)}, \quad P = \frac{\sum I(00l)}{\sum I(hkl)} \quad (2)$$

where $\sum I_0(hkl)$ and $\sum I(hkl)$ are the total of all relative intensities of (hkl) for randomly and preferentially oriented samples, respectively.[53] The high F value indicates the high orientation degree of the grains. As shown in Table 1, the orientation factor $F(400)$ increases from 0.26 for the initial sample to 0.50 for the $Na_{0.03}Sn_{0.97}Se$–5%Te sample, indicating that the LPHD process enhance the texture for the compressed samples. However, with more element Te added to liquid-phase sintering, the $F(400)$ value of the $Na_{0.03}Sn_{0.97}Se$–15%Te sample decreases to 0.32.

To further examine the textured structure, the SEM microscopic characterizations of the $Na_{0.03}Sn_{0.97}Se$–x%Te (x = 0, 5 and 15) LPHD samples are presented in Fig. 2. The initial $Na_{0.03}Sn_{0.97}Se$ sample without the addition of Te exhibits disorderedness and less orientation, similar to most polycrystalline SnSe after the HP process.[54,55] However, the grains of the LPHD samples were refined and aligned in order, consistent with the enhanced orientation factor $F(400)$ values.[41,43,44] On the one hand, the liquid Te promotes the crystal plane slipping and preferred orientation during the sintering process. On the other hand, the hot deformation process boosts the inversion and recrystallization of the grains. Thus, the combined process of the LPHD technique can enhance the degree of texture of the SnSe-based material effectively. The grain size of the LPHD samples increased significantly compared with the initial sample, in particular, the $Na_{0.03}Sn_{0.97}Se$–5%Te sample possessed the largest average grain size. Such a phenomenon was also observed in previous reports about SnSe and other layered TE materials,[56–58] and it was closely related to the electronic properties.

Furthermore, the compositional homogeneity of the sample was confirmed by the back scattered electron image and EDS results shown in Fig. S3 in the ESI.† The results of $Na_{0.03}Sn_{0.97}Se$–15%Te indicated that the content of Na is much lower than the nominal one and a thimbleful of Te is also observed in the lattice, consistent with the above XRD results.

3.2 Electronic transport properties

The electronic transport properties of all samples perpendicular to the pressing direction are summarized in Fig. 3. Fig. 3a shows the temperature-dependent electrical conductivity σ of the $Na_{0.03}Sn_{0.97}Se$ polycrystalline samples. For LPHD samples, σ firstly decreased with increasing temperature until ~670 K and then increased slightly, similar to the changing tendency of the single crystal.[25,27] It can be seen that the LPHD technique significantly improved the σ of the $Na_{0.03}Sn_{0.97}Se$–x%Te samples near room temperatures. Especially for x = 5, the σ reached a maximum value of 218 S cm^{-1} at 303 K. Compared to the results of HD and LPS methods, the σ of the LPHD sample increased by about 50% and 30%, respectively.[43,44] Moreover, the LPHD samples exhibited excellent electrical properties during the whole temperature range. For example, the σ of the $Na_{0.03}Sn_{0.97}Se$–5%Te sample at 810 K was 74 S cm^{-1}, which was still higher than those of other polycrystalline SnSe.[31,34,35,55]

Fig. 3b and Table 2 present the room temperature carrier concentration (n) and carrier mobility (μ_H) of the LPHD samples. Similar to the results of previous HD and LPS samples,[43,44] the carrier concentrations of the LPHD samples increased slightly and remained at a relatively stable level, mainly owing to the residual Te dopants that generated Sn vacancies.[59,60]

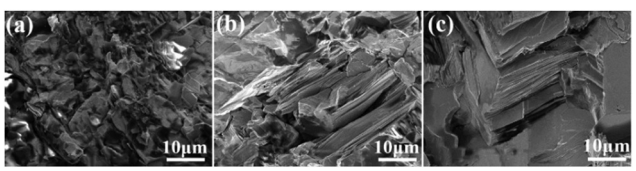

Fig. 2 The SEM image of the fractured surfaces parallel to the pressure direction for the $Na_{0.03}Sn_{0.97}Se$–x%Te samples with (a) x = 0, (b) x = 5, and (c) x = 15.

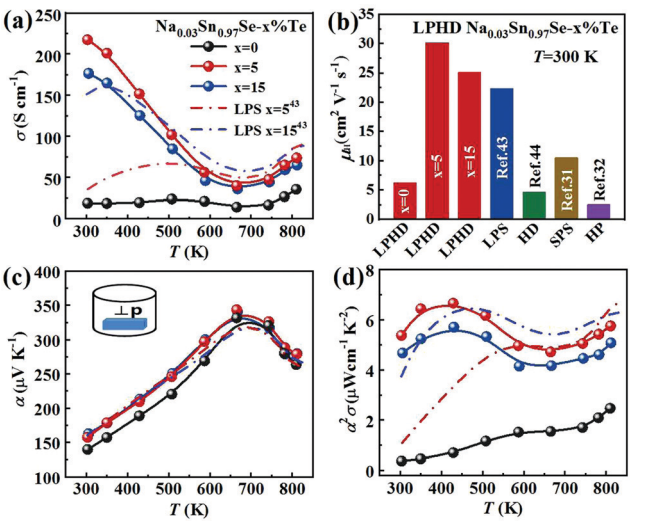

Fig. 3 Temperature dependence of $Na_{0.03}Sn_{0.97}Se$–x%Te (x = 0, 5 and 15) LPHD samples: (a) electrical conductivity, (b) room temperature Hall mobility with some previous reports as a comparison, (c) Seebeck coefficient and (d) power factor.

Table 2 The density (ρ), carrier concentration (n), Hall mobility (μ_H), and the Seebeck coefficient (α) at 300 K for polycrystalline $Na_{0.03}Sn_{0.97}Se$ samples prepared using different processes

Methods	ρ (g cm^{-3})	n (10^{19} cm^{-3})	μ_H (cm^2 V^{-1} s^{-1})	α (μV K^{-1})
ZM	6.04	0.051	166	—
HD	5.72	2.67	4.7	198
LPS	6.03	3.16	22.3	145
LPHD-0%Te	5.76	1.89	6.2	139
LPHD-5%Te	6.03	4.51	30.1	158
LPHD-15%Te	6.08	4.39	25.1	163

More importantly, the room temperature carrier mobility improved significantly due to the enhancement of the texture degree. It can be seen that the carrier mobility increases obviously from 6.2 to 30.1 cm^2 V^{-1} s^{-1} of LPHD–5%Te, which is much higher than those of LPS[43] and HD samples.[44] A rapidly increased mobility was also observed in previous reports, and it may be due to the barrier-like scattering originated from oxidation, defects or impurities at the grain boundaries of SnSe materials.[61–63] The liquid Te may fill the grain gaps and thus reduce the oxidation and defects at the grain boundaries. Additionally, the stress induced by plastic deformation could be released in a timely manner by the extrusion of liquid Te during the HD process. As a result, the weakened grain boundary scattering by the LPHD process significantly improves the carrier mobility. Nevertheless, too much liquid Te (such as 15%Te) would wrap and lubricate the crystal grains, leading to a lower reduction in carrier mobility unexpectedly. As discussed above, the LPHD process enlarged the grain size and the corresponding texture degree was significantly raised (see the F values in Table 1), which were beneficial for the carrier mobility and electrical conductivity.

Fig. 3c shows the temperature dependence of Seebeck coefficient (α). The relatively high α of all samples were positive, exhibiting p-type transport behavior. With the increasing temperature, the Seebeck coefficients first increased to the maximum and then decreased. The peak value was 327 μV K^{-1} at 680 K obtained in $Na_{0.03}Sn_{0.97}Se$–5%Te. Above 680 K, the reduction of α in all samples could be attributed to the thermal excitation of minority carriers (bipolar effect). Compared to the sample without Te addition, the α of $Na_{0.03}Sn_{0.97}Se$–x%Te increased obviously. It may be a result of the suppression of bipolar effect with improved carrier concentration.[43,52]

As shown in Fig. 3d, the LPHD samples exhibited a much higher PF ($\alpha^2\sigma$) than the LPS one due to the significantly increased electrical conductivity. The maxima of $\alpha^2\sigma$ were found to be 6.65 μW cm^{-1} K^{-2} at 430 K and 5.75 μW cm^{-1} K^{-2} at 830 K for $Na_{0.03}Sn_{0.97}Se$–5%Te. It is worth noting that the PF value at room temperature is 5.38 μW cm^{-1} K^{-2}, which is the highest value observed in SnSe-based materials except for SnSe single crystals. Due to the enhanced texture degree, the PF of all LPHD samples were maintained at higher values in the whole temperature range, particularly for $Na_{0.03}Sn_{0.97}Se$–5%Te. The average PF_{ave} of $Na_{0.03}Sn_{0.97}Se$–5%Te was 5.62 μW cm^{-1} K^{-2}, which was much higher than most p-type polycrystalline SnSe.[32,44,60,64] Such enhanced $\alpha^2\sigma$ was mainly attributed to the optimized texture degree and significantly improved electrical properties during the LPHD process.

3.3 Thermal conductivity and *ZT* value

Fig. 4a presents the total thermal conductivity κ of all samples as functions of temperature. All the κ gradually reduced with increasing temperature and then an upturn appeared around 743 K, arising from the *Pnma–Cmcm* phase transition. The LPHD samples, especially the $Na_{0.03}Sn_{0.97}Se$–5%Te one, exhibited a lower κ than the one without excess Te in the whole temperature range. It is worthy to note that κ was significantly suppressed during the combined LPHD process as compared with the LPS method under the same condition.[43] The lowest κ value was 0.45 W m^{-1} K^{-1} at 743 K for the $Na_{0.03}Sn_{0.97}Se$–5%Te LPHD sample.

The electronic thermal conduction κ_e (see Fig. S4 of the ESI†) is proportional to σ according to the Wiedemann–Franz law $\kappa_e = LT\sigma$, where the Lorenz number L was calculated by fitting the respective Seebeck coefficient values to the reduced chemical potential. Then, the lattice thermal conduction κ_l was evaluated by $\kappa_l = \kappa - \kappa_e$. Fig. 4b presents the temperature-dependent κ_l of the LPHD and previous LPS samples.[43] Very different from the previously reported LPS samples with the addition of Te, the κ_l of the LPHD samples was obviously lower in the whole temperature range, which was mainly due to the introduced defects during the plastic deformation. As shown, the lowest κ_l value was obtained as 0.40 W m^{-1} K^{-1} in the x = 5 LPHD sample at 743 K.

To better understand the reduced κ_l of the LPHD samples, TEM analysis was carried out on the $Na_{0.03}Sn_{0.97}Se$–x%Te (x = 0, 5) samples. Mesoscale grains with sizes around 0.5–1 μm were observed in the sample as shown in Fig. 5a (x = 0) and b (x = 5). It can be clearly seen that the typical areas in Fig. 5b marked as 1 and 2 possess many strain-field domains, which were ascribed to a dislocation effect in the previous report.[65] The high-resolution TEM (HRTEM) image of region 1 in Fig. 5b was shown in Fig. 5c. Fig. 5d presents the inverse Fourier transformation (IFFT) image along the (400) plane reflections of the red box region in Fig. 5c, in which many dislocation defects can be readily observed. Moreover, interface regions with selenium precipitates and a $SnSe_2$ second phase embedded in the matrix can be seen from the HRTEM images and EDS results shown in Fig. S6 and Table S1 in the ESI.† These emerged phonon

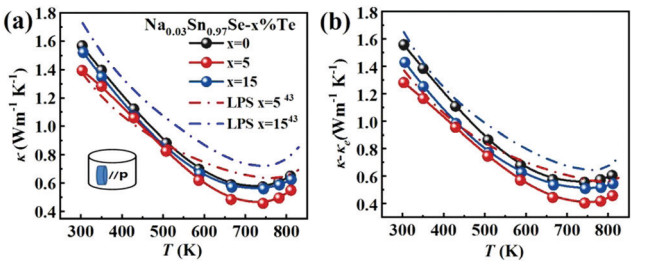

Fig. 4 Temperature dependences of (a) thermal conductivity; (b) lattice thermal conductivity. The data for the LPS samples are plotted for comparison.[43]

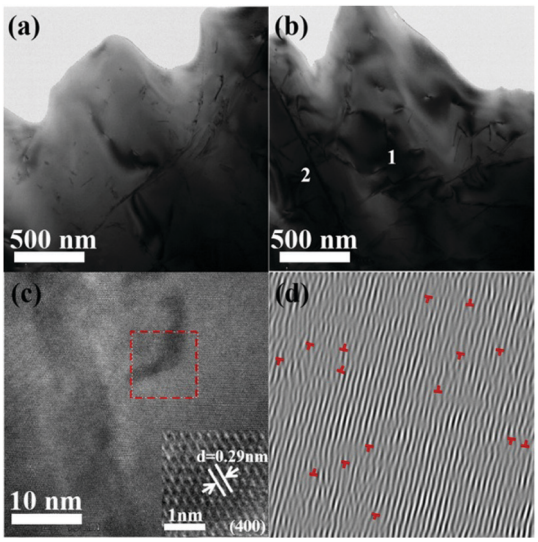

Fig. 5 Microstructure of the LPHD samples: (a) low-magnification TEM image of $Na_{0.03}Sn_{0.97}Se$-0%Te; (b) low-magnification TEM image of $Na_{0.03}Sn_{0.97}Se$–5%Te with the defects in the matrix; (c) HRTEM image from (b) the region marked 1 with the FFT image and its interplanar spacing; (d) inverse FFT image of the red box in panel (c) obtained from the (400) reflection.

scattering centers during the LPHD process may strengthen the phonon scattering and decrease the κ_l. Additionally, similar to many previous LPS results of Bi_2Te_3 and SnSe,[42,43,52] excess Te addition led to a slightly increased κ_l in the $Na_{0.03}Sn_{0.97}Se$–x%Te samples, which needs further investigation in the future.

Fig. 6a displays the temperature dependence of ZT values for all samples. As shown, the ZTs were roughly increased with the increasing temperature. The maximum ZT value was 0.9 at 780 K for the $Na_{0.03}Sn_{0.97}Se$–5%Te sample. Since the PFs were limited at a higher temperature, such a peak ZT was not very competitive compared with those inrevious reports.[19,20,36,44] However, compared with the results of normal LPS or HD methods, a higher averaged ZT value (ZT_{ave}) was achieved using the LPHD technique as summarized in Fig. 6b. Between the temperature range of 300 to 810 K, our LPHD-prepared polycrystalline $Na_{0.03}Sn_{0.97}Se$ exhibited a ZT_{ave} of 0.49, which was obviously higher than the previous reported $Na_{0.03}Sn_{0.97}Se$ polycrystalline samples.[31,32,43,44,60] The improved ZTs at a lower temperature resulted from both the high carrier mobility in a more textured structure and the obvious reduction of κ_l by the enhanced phonon scattering.

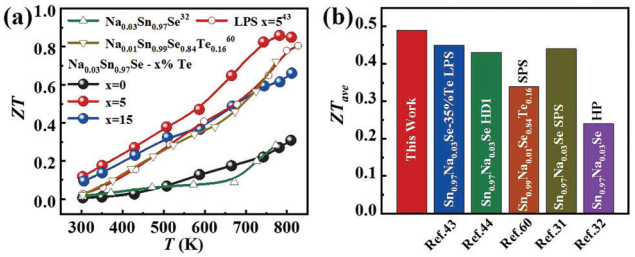

Fig. 6 (a) Temperature dependence of ZT for LPHD samples; (b) average ZT values from 300 to 810 K for our $Na_{0.03}Sn_{0.97}Se$–5%Te LPHD sample and other previously reported polycrystalline $Na_{0.03}Sn_{0.97}Se$ samples.[31,32,43,44,60]

4. Conclusions

In summary, polycrystalline $Na_{0.03}Sn_{0.97}Se$–x%Te (x = 0, 5 and 15) samples were successfully prepared using a convenient and low-cost LPHD technique, which combined the advantages of the LPS and HD processes. For the electronic transport, the texture of the sample was significantly enhanced and the grains showed a strong orientation along the (400) plane. The carrier mobility was effectively boosted, leading to a higher electrical conductivity and power factor around room temperature. For the phonon transport, dense dislocation defects and $SnSe_2$ precipitates emerged during the LPHD process. These defects increased the phonon scattering rate and obviously reduced the lattice thermal conductivity. With these synergistical effects, a maximum ZT of 0.9 at 780 K and an average ZT value of 0.49 between 300 and 810 K were obtained in the $Na_{0.03}Sn_{0.97}Se$–5%Te LPHD materials. This work provides a novel technique for realizing high thermoelectric performance in SnSe-based materials through texture modification.

Conflicts of interest

There are no conflicts to declare.

Acknowledgements

This study was supported by the National Science Foundation of China (51872301 and 21875273), the Natural Science Foundation of Zhejiang Province (LY18A040008), and the Youth Innovation Promotion Association of Chinese Academy of Sciences (2019298).

References

1 D. M. Rowe, *Thermoelectric and Its Energy Harvesting*, CRC Press, 2012.
2 L. E. Bell, *Science*, 2008, **321**, 1457–1461.
3 Y. Zheng, Y. Luo, C. Du, B. Zhu, Q. Liang, H. H. Hng, K. Hippalgaonkar, J. Xu and Q. Yan, *Mater. Chem. Front.*, 2017, **1**, 2457–2473.
4 A. Sorkina and S. Adams, *Mater. Adv.*, 2020, **1**, 184–196.
5 W. S. Liu and S. Q. Bai, *J. Materiomics*, 2019, **5**, 321–336.
6 G. J. Tan, L. D. Zhao and M. G. Kanatzidis, *Chem. Rev.*, 2016, **116**, 12123–12149.
7 W. Liu, H. S. Kim, Q. Jie and Z. Ren, *Sci. Mater.*, 2016, **112**, 3269–3274.
8 C. H. Lee, M. H. Ma, W. H. Li, P. C. Wei, Y. Y. Chen, Y. Zhao and J. W. Lynn, *Mater. Today Phys.*, 2019, **11**, 100171.
9 J. P. Heremans, V. Jovovic, E. S. Toberer, A. Saramat, K. Kurosaki, A. Charoenphakdee, S. Yamanaka and G. J. Snyder, *Science*, 2008, **321**, 554–557.

10 Y. X. Chen, Z. H. Ge, M. J. Yin, D. Feng, X. Q. Huang, W. Y. Zhao and J. Q. He, *Adv. Funct. Mater.*, 2016, **26**, 6836–6845.
11 Y. Pei, X. Shi, A. LaLonde, H. Wang, L. Chen and G. J. Snyder, *Nature*, 2011, **473**, 66–69.
12 X. J. Tan, H. X. Wang, G. Q. Liu, J. G. Noudem, H. Y. Hu, J. T. Xu, H. Z. Shao and J. Jiang, *Mater. Today*, 2018, **7**, 35–44.
13 L. S. Mao, Y. N. Yin, Q. Zhang, G. Q. Liu, H. X. Wang, Z. Guo, H. Y. Hu, Y. K. Xiao, X. J. Tan and J. Jiang, *Energy Environ. Sci.*, 2020, **13**, 616–621.
14 H. R. Yang, J. H. Bahk, T. Day, A. M. S. Mohammed, G. J. Snyder, A. Shakouri and Y. Wu, *Nano Lett.*, 2015, **15**, 1349–1355.
15 Z. Zhou, J. Yang, Q. Jiang, D. Zhang, J. Xin, X. Li, Y. Ren and X. He, *J. Am. Chem. Soc.*, 2017, **100**, 5723.
16 K. Biswas, J. He, I. D. Blum, C. I. Wu, T. P. Hogan, D. N. Seidman, V. P. Dravid and M. G. Kanatzidis, *Nature*, 2012, **489**, 414–418.
17 T. Zhu, Y. Liu, C. Fu, J. P. Heremans, J. G. Snyder and X. Zhao, *Adv. Mater.*, 2017, **29**, 1605884.
18 N. Neophytou, S. Foster, V. Vargiamidis, G. Pennelli and D. Narducci, *Mater. Today Phys.*, 2019, **11**, 100159.
19 Y. B. Luo, S. T. Cai, X. Hua, H. J. Chen, Q. H. Liang, C. F. Du, Y. Zheng, J. H. Shen, J. W. Xu, C. Wolverton, V. P. Dravid, Q. Y. Yan and M. G. Kanatzidis, *Adv. Energy Mater.*, 2018, **9**, 1803072.
20 M. M. Li, H. Z. Shao, J. T. Xu, Q. S. Wu, X. J. Tan, G. Q. Liu, M. Jin, H. Y. Hu, H. J. Huang, J. F. Zhang and J. Jiang, *J. Materiomics*, 2018, **4**, 321–328.
21 Z. Chen, B. Ge, W. Li, S. Lin, J. Shen, Y. Chang, R. Hanus, G. J. Snyder and Y. Pei, *Nat. Commun.*, 2017, **8**, 13828–13836.
22 Y. K. Xiao, G. X. Chen, H. M. Qin, M. L. Wu, Z. P. Xiao, J. Jiang, J. T. Xu, H. C. Jiang and G. J. Xu, *J. Mater. Chem. A*, 2014, **2**, 8512–8516.
23 R. Guo and S. Lee, *Mater. Today Phys.*, 2019, **12**, 100177.
24 C. W. Li, J. Hong, A. F. May, D. Bansal, S. Chi, T. Hong, G. Ehlers and O. Delaire, *Nat. Phys.*, 2015, **11**, 1063–1071.
25 K. L. Peng, X. Lu, H. Zhan, S. Hui, X. D. Tang, G. W. Wang, J. Y. Dai, C. Uher, G. Y. Wang and X. Y. Zhou, *Energy Environ. Sci.*, 2016, **9**, 454–460.
26 J. Hong and O. Delaire, *Mater. Today Phys.*, 2019, **10**, 100093.
27 L. D. Zhao, S. H. Lo, Y. Zhang, H. Sun, G. Tan, C. Uher, C. Wolverton, V. P. Dravid and M. G. Kanatzidis, *Nature*, 2014, **508**, 373–390.
28 C. Chang, M. Wu, D. He, Y. Pei, C.-F. Wu, X. Wu, H. Yu, F. Zhu, K. Wang, Y. Chen, L. Huang, J. F. Li, J. He and L. D. Zhao, *Science*, 2018, **360**, 778.
29 C. L. Chen, H. Wang, Y. Y. Chen, T. Day and G. J. Snyder, *J. Mater. Chem. A*, 2014, **2**, 11171–11176.
30 S. Li, Y. M. Wang, C. Chen, X. Li, W. Xue, X. Wang, Z. Zhang, F. Cao, J. Sui, X. Liu and Q. Zhang, *Adv. Sci.*, 2018, **5**, 1800598.
31 K. Peng, H. Wu, Y. C. Yan, L. J. Guo, G. Y. Wang, X. Lu and X. Y. Zhou, *J. Mater. Chem. A*, 2017, **5**, 14053–14060.
32 E. K. Chere, Q. Zhang, K. Dahal, F. Cao, J. Mao and Z. Ren, *J. Mater. Chem. A*, 2016, **4**, 1848–1854.
33 Y. H. Zhu, J. Carrete, Q. L. Meng, Z. W. Huang, N. Mingo, P. Jiang and X. H. Bao, *J. Mater. Chem. A*, 2018, **6**, 7959–7966.
34 N. K. Singh, S. Bathula, B. Gahtori, K. Tyagi, D. Haranath and A. Dhar, *J. Alloys Compd.*, 2016, **668**, 152–158.
35 D. B. Li, X. J. Tan, J. T. Xu, G. Q. Liu, M. Jin, H. Z. Shao, H. J. Huang, J. F. Zhang and J. Jiang, *RSC Adv.*, 2017, **7**, 17906–17912.
36 D. Li, J. C. Li, X. Y. Qin, J. Zhang, H. X. Xin, C. J. Song and L. Wang, *Energy*, 2016, **116**, 861–866.
37 F. Li, W. T. Wang, Z. H. Ge, Z. H. Zheng, J. T. Luo, P. Fan and B. Li, *Materials*, 2018, **11**, 203–213.
38 Y. W. Li, F. Li, J. F. Dong, Z. H. Ge, F. Y. Kang, J. Q. He, H. D. Du, B. Li and J. F. Li, *J. Mater. Chem. C*, 2016, **4**, 2047–2055.
39 D. Feng, Z. H. Ge, D. Wu, Y. X. Chen, T. T. Wu, J. Li and J. Q. He, *Phys. Chem. Chem. Phys.*, 2016, **18**, 31821–31827.
40 X. Wang, J. T. Xu, G. Q. Liu, Y. J. Fu, Z. Liu, X. J. Tan, H. Z. Shao, H. C. Jiang, T. Y. Tan and J. Jiang, *Appl. Phys. Lett.*, 2016, **108**, 083902.
41 Y. J. Fu, J. T. Xu, G. Q. Liu, J. K. Yang, X. J. Tan, Z. Liu, H. M. Qin, H. Z. Shao, H. C. Jiang, B. Liang and J. Jiang, *J. Mater. Chem. C*, 2016, **4**, 1201–1207.
42 S. I. Kim, K. H. Lee, H. A. Mun, H. S. Kim, S. W. Hwang, J. W. Roh, D. J. Yang, W. H. Shin, X. S. Li, Y. H. Lee, G. J. Snyder and S. W. Kim, *Science*, 2015, **348**, 109–114.
43 J. H. Zhang, J. Xu, X. J. Tan, H. X. Wang, G. Q. Liu, H. Z. Shao, B. Yu, S. Yue and J. Jiang, *J. Mater. Chem. C*, 2019, **7**, 2653–2658.
44 S. J. Liang, J. T. Xu, J. G. Noudem, H. X. Wang, X. J. Tan, G. Q. Liu, H. Z. Shao, B. Yu, S. Yue and J. Jiang, *J. Mater. Chem. A*, 2018, **6**, 23730–23735.
45 L. P. Hu, H. J. Wu, T. J. Zhu, C. G. Fu, J. Q. He, P. J. Ying and X. B. Zhao, *Adv. Energy Mater.*, 2015, **5**, 1500411.
46 R. S. Zhai, L. P. Hu, H. J. Wu, Z. J. Xu, T. J. Zhu and X. B. Zhao, *ACS Appl. Mater. Interfaces*, 2017, **9**, 28577–28585.
47 C. Tan, X. J. Tan, B. Yu, G. Q. Liu, H. X. Wang, G. Q. Luo, J. T. Xu, Q. S. Wu, B. Liang and J. Jiang, *ACS Appl. Energy Mater.*, 2019, **2**, 6714–6719.
48 F. Li, R. S. Zhai, Y. H. Wu, Z. J. Xu, X. B. Zhao and T. J. Zhu, *J. Materiomics*, 2018, **4**, 208–214.
49 Y. Liu, Y. Zhang, S. Ortega, M. Ibanez, K. H. Lim, A. Grau-Carbonell, S. Marti-Sanchez, K. M. Ng, J. Arbiol, M. V. Kovalenko, D. Cadavid and A. Cabot, *Nano Lett.*, 2018, **18**, 2557–2563.
50 C. H. Zhang, M. D. L. Mata, Z. Li, F. J. Belarre, J. Arbiol, K. A. Khor, D. Poletti, B. B. Zhu, Q. Y. Yan and Q. H. Xiong, *Nano Energy*, 2016, **30**, 630–638.
51 R. Deng, X. Su, Z. Zheng, W. Liu, Y. Yan, Q. Zhang, V. P. Dravid, C. Uher, M. G. Kanatzidis and X. Tang, *Sci. Adv.*, 2018, **4**, eaar5606.
52 Y. H. Wu, Y. Yu, Q. Zhang, Ti. J. Zhu, R. S. Zhai and X. B. Zhao, *Adv. Sci.*, 2019, **6**, 1901702.
53 F. K. Lotgering, *J. Inorg. Nucl. Chem.*, 1960, **16**, 100–108.
54 T. R. Wei, G. Tan, X. Zhang, C. F. Wu, J. F. Li, V. P. Dravid, G. J. Snyder and M. G. Kanatzidis, *J. Am. Chem. Soc.*, 2016, **138**, 8875–8882.

55 Y. M. Han, J. Zhao, M. Zhou, X. X. Jiang, H. Q. Leng and L. F. Li, *J. Mater. Chem. A*, 2015, **3**, 4555–4559.
56 D. Kenfaui, D. Chateigner, M. Gomina and J. G. Noudem, *J. Alloys Compd.*, 2010, **490**, 472–479.
57 L. P. Hu, X. H. Liu, H. H. Xie, J. J. Shen, T. J. Zhu and X. B. Zhao, *Acta Mater.*, 2012, **60**, 4431–4437.
58 H. Mun, K. H. Lee, S. J. Yoo, H. S. Kim, J. Jeong, S. H. Oh, G. J. Snyder, Y. H. Lee, Y. M. Kim and S. W. Kim, *Acta Mater.*, 2018, **159**, 266–275.
59 M. Hong, Z. G. Chen, L. Yang, T. C. Chasapis, S. D. Kang, Y. Zou, G. J. Auchterlonie, M. G. Kanatzidis, G. J. Snyder and J. Zou, *J. Mater. Chem. A*, 2017, **5**, 10713–10721.
60 T. R. Wei, C. F. Wu, X. Z. Zhang, Q. Tan, L. Sun, Y. Pan and J. F. Li, *Phys. Chem. Chem. Phys.*, 2015, **17**, 30102–30109.
61 Z. H. Ge, D. S. Song, X. Y. Chong, F. S. Zheng, L. Jin, X. Qian, L. Zheng, R. E. Dunin-Borkowski, P. Qin, J. Feng and L. D. Zhao, *J. Am. Chem. Soc.*, 2017, **139**, 9714–9720.
62 Y. K. Lee, K. Ahn, J. Cha, C. J. Zhou, H. S. Kim, G. Choi, S. I. Chae, J. H. Park, S. P. Cho, S. H. Park, Y. E. Sung, W. B. Lee, T. Hyeon and I. Chung, *J. Am. Chem. Soc.*, 2017, **139**, 10887–10896.
63 S. Wang, S. Hui, K. L. Peng, T. P. Bailey, X. Y. Zhou, X. F. Tang and C. Uher, *J. Mater. Chem. C*, 2017, **5**, 10191–10200.
64 S. S. Sassi, C. Candolfi, J. B. Vaney, V. Ohorodniichuk, P. Masschelein, A. Dauscher and B. Lenoir, *Appl. Phys. Lett.*, 2014, **104**, 212105.
65 D. Maier, *Solid State Commun.*, 2002, **122**, 565.

